

1 **A set of methods to evaluate the below-cloud evaporation effect on local**
2 **precipitation isotopic composition: a case study for Xi'an, China**

3 Meng Xing^{1,2*}, Weiguo Liu^{1,2,3*}, Jing Hu^{1,2}, Zheng Wang^{1,2}

4

5

6 1. State Key Laboratory of Loess and Quaternary Geology, Institute of Earth
7 Environment, Chinese Academy of Sciences, Xi'an, 710061, China

8 2. CAS Center for Excellence in Quaternary Science and Global Change, Xi'an,
9 710061, China.

10 3. University of Chinese Academy of Sciences, Beijing, 100049, China

11

12 Corresponding authors:

13 Meng Xing email address: xingmeng@ieecas.cn

14 Weiguo Liu email address: liuwg@loess.llqg.ac.cn

15

16

17

18

19

20

21

22

23

24

25

26

27

28

29

30

31

32 Abstract:

33 When hydrometeors fall from an in-cloud saturated environment toward the ground,
34 especially in arid and semiarid regions, below-cloud processes may heavily alter the
35 isotopic composition of precipitation through equilibrium and non-equilibrium
36 fractionations. If these below-cloud processes are not correctly identified, they can lead
37 to misinterpretation of the precipitation isotopic signal. To correctly understand the
38 environmental information recorded in the precipitation isotopes, qualitatively
39 analyzing the below-cloud processes and quantitatively calculating the below-cloud
40 evaporation effect are two important steps. Here, based on two years of synchronous
41 observations of precipitation and water vapor isotopes in Xi'an, we compiled a set of
42 effective methods to systematically evaluate the below-cloud evaporation effect on
43 local precipitation isotopic composition. The $\Delta d\Delta\delta$ -diagram is a tool to effectively
44 diagnose below-cloud processes, such as equilibration or evaporation, because the
45 isotopic differences ($\delta^2\text{H}$, d-excess) between the precipitation-equilibrated vapor and
46 the observed vapor show different pathways. By using the $\Delta d\Delta\delta$ -diagram, our data
47 show that evaporation is the major below-cloud process in Xi'an, while snowfall
48 samples retain the initial cloud signal because they are less impacted by the isotopic
49 exchange between vapor and solid phases. Then, we chose two methods to
50 quantitatively characterize the influence of below-cloud evaporation on local
51 precipitation isotopic composition: one is based on the raindrop's mass change during
52 its falling (hereafter referred to as method 1); the other is dependent on the variations
53 in precipitation isotopic composition from the cloud base to the ground (hereafter
54 referred to as method 2). By comparison, we found that there are no significant
55 differences between the two methods in evaluating the evaporation effect on $\delta^2\text{H}_p$,
56 except for snowfall events. The slope of evaporation proportion to the variation in $\delta^2\text{H}$
57 ($F_i/\Delta\delta^2\text{H}$) is slightly larger in method 1 (1.0 ‰/‰) than in method 2 (0.9 ‰/‰).
58 Additionally, both methods indicate that the evaporation effect is weak in autumn and
59 heavy in spring. Through a sensitivity test, we found that in two methods, relative
60 humidity is the most sensitive parameter, while the temperature shows different effects
61 on the two methods. Therefore, we concluded that both methods are suited to
62 investigate the below-cloud evaporation effect, while in method 2, other below-cloud
63 processes, such as supersaturation, can still be included. By applying method 2, the
64 diagnosis of below-cloud processes and the understanding of their effects on the
65 precipitation isotopic composition will be improved.

66

67

68 **1 Introduction**

69 For the paleoenvironment, the isotopic signal of precipitation recorded in ice cores
70 (Thompson et al., 2000; Yao et al., 1996), tree rings (Liu et al., 2004; Liu et al., 2017b),
71 speleothems (Cai et al., 2010; Tan et al., 2014), and leaf wax of loess-paleosol
72 deposits (Wang et al., 2018b) and lake sediments (Liu et al., 2017a, 2019) could be
73 used to reconstruct the information of temperature, precipitation, and hydrological
74 regimes in geologic history, as it had participated in the formation or growth of these
75 geological archives. For the modern environment, it could be used to quantitatively
76 constrain the water vapor contribution from the end-members of advection (Peng et al.,
77 2011), evaporation (Sun et al., 2020; Wang et al., 2016a), transpiration (Li et al., 2016;
78 Zhao et al., 2019), and even anthropogenic activities (Fiorella et al., 2018; Gorski et
79 al., 2015; Xing et al., 2020), as it is itself an important part of the hydrological cycle.
80 Thus, the hydrogen and oxygen isotopes of precipitation are some of the most
81 important tools to trace the hydrological cycle and climate change (Bowen et al., 2019;
82 Gat, 1996). However, limited by the sampling and isotopic fractionation theories, there
83 remains large uncertainty (i.e., the below-cloud evaporation intensity, the moisture
84 recycling ratio, water molecule exchange between the droplet and ambient air, etc.) in
85 deciphering the information contained in precipitation when using hydrogen and
86 oxygen isotopes (Bowen et al., 2019; Yao et al., 2013).

87

88 Below-cloud evaporation is one of the processes that influences the falling raindrops
89 and modifies their final stable isotopic content and thus needs to be properly evaluated.
90 Over the past decades, to determine whether a hydrometeor has evaporated during
91 its fall, most studies have depended on a second-order isotopic parameter (Dansgaard,
92 1964; Jeelani et al., 2018; Li and Garzzone, 2017), deuterium excess (defined as d-
93 excess= $\delta^2\text{H}-8\times\delta^{18}\text{O}$). This parameter is representative of the non-equilibrium
94 fractionations, since light isotopes (^1H and ^{16}O) equilibrate faster than heavy isotopes
95 (^2H and ^{18}O) in different phases (Clark and Fritz, 1997; Dansgaard, 1964). For
96 raindrops, the lighter water molecules ($^1\text{H}_2^{16}\text{O}$) preferentially equilibrate or diffuse from
97 the liquid phase to the gas phase during their falling through unsaturated ambient air.
98 Equilibrium fractionation does not substantially change d-excess, while a non-
99 equilibrium diffusional process would result in a decrease in d-excess in rain (Fisher,
100 1991; Merlivat and Jouzel, 1979). Additionally, the slope of the local meteoric water
101 line (LMWL) has also been widely used as a metric to infer the below-cloud evaporation
102 effect according to the theory of water isotope equilibrium fractionation (Chakraborty
103 et al., 2016; Putman et al., 2019b; Wang et al., 2018a). Generally, the LMWL slope is

104 approximately equal to 8.0 in equilibrium fractionation, and a slope deviating from 8.0
105 is related to non-equilibrium fractionation, such as the re-evaporation of raindrops.

106

107 However, it is worth noting that the change in air masses (Guan et al., 2013),
108 condensation under supersaturation conditions (Jouzel et al., 2013), or moisture
109 exchange in the cloud and subcloud layers (Graf et al., 2019) also cause large
110 variations in the slopes and d-excess values (Putman et al., 2019a; Tian et al., 2018).
111 Therefore, it is imperative to explore a novel method to more accurately identify the
112 below-cloud processes. Recently, Graf et al. (2019) provided a new interpretive
113 framework to directly separate the convoluted influences on the stable isotopic
114 composition of vapor and precipitation according to the theoretical fractionation
115 processes, especially the influences of equilibration and below-cloud evaporation. The
116 axes of the new diagram consist of the differences, $\Delta\delta^2\text{H}$ and Δd , between the isotopic
117 composition of equilibrated vapor from precipitation and near-surface observed vapor,
118 namely, the $\Delta\delta\Delta d$ -diagram. Compared with the slope of the LMWL or d-excess, below-
119 cloud equilibration and evaporation have different spatial distributions in the two-
120 dimensional phase space of the $\Delta\delta\Delta d$ -diagram, which makes them more easily
121 distinguishable. Although the $\Delta\delta\Delta d$ -diagram gives us a new guideline to more
122 accurately identify below-cloud processes, Graf's et al. (2019) work was only tested on
123 a cold frontal rain event during a short time, and hence, more work needs to be done
124 to validate the general applicability of their framework.

125

126 The cloud-base signal of precipitation isotopes is important in hydrological studies, and
127 thus it is necessary to quantitatively evaluate the influence of below-cloud evaporation
128 on its variations. Normally, the isotopic difference of raindrops between ground level
129 and cloud base is determined by the below-cloud evaporation intensity. Because it is
130 difficult to accurately measure the vapor or precipitation isotopic composition at the
131 cloud base, the model proposed by Stewart (1975) has been widely used to evaluate
132 the below-cloud evaporation effect for a long time. Based on well-defined laboratory
133 conditions, Stewart (1975) parameterized the change in the isotopic composition of a
134 falling water drop with the vapor and raindrop isotopic compositions at the cloud base
135 and the remaining fraction of raindrop mass after evaporation (hereafter referred to as
136 method 1). Froehlich et al. (2008) adapted the Stewart model and then assessed the
137 change in d-excess due to below-cloud evaporation in the European Alps. Wang et al.
138 (2016b) further refined the calculations of the parameters, which are used to determine
139 the remaining fraction of raindrop mass in the Stewart model, to assess the variation

140 in d-excess of raindrops in central Asia. However, these quantitative evaluations of
141 below-cloud evaporation are indirect because the results are largely dependent on the
142 parameter that is the remaining fraction of raindrop mass after evaporation.

143

144 In recent years, with progress in optical laser systems, relatively portable field-
145 deployable laser spectroscopic instruments have emerged, which allows online,
146 autonomous, and high-frequency site measurements of the water vapor stable isotope
147 composition to be achieved (Aemisegger et al., 2012; Christner et al., 2018). Therefore,
148 the vapor or precipitation isotopic composition at the cloud base could be directly
149 measured (Salmon et al., 2019) or indirectly deduced from the ground-level vapor
150 isotopic composition (Deshpande et al., 2010; Salamalikis et al., 2016). This enables
151 us to directly calculate the influence of below-cloud processes on the precipitation
152 isotopic composition (hereafter referred to as method 2). However, thus far, these have
153 not been systematically compared.

154

155 Here, we use measurements of two-year near-ground water vapor isotope
156 compositions and 141 precipitation isotope compositions (including event-based
157 snowfall samples) that were collected in Xi'an (34.23°N, 108.88°E), Shaanxi Province,
158 located in the Chinese Loess Plateau (CLP). The objectives of this study are to: 1.
159 qualitatively identify the below-cloud processes of falling raindrops by using the $\Delta\delta\Delta d$ -
160 diagram; 2. quantitatively evaluate the below-cloud evaporation effect on precipitation
161 isotopic composition by two methods and compare their differences; 3. understand the
162 role of meteorological factors on below-cloud evaporation and the characteristics of
163 below-cloud evaporation in Xi'an city. Therefore, with the advantages of paired
164 observations of vapor and precipitation isotopes near the ground, this study will
165 compile a set of effective methods to evaluate the below-cloud evaporation effect on
166 the local precipitation isotopic composition.

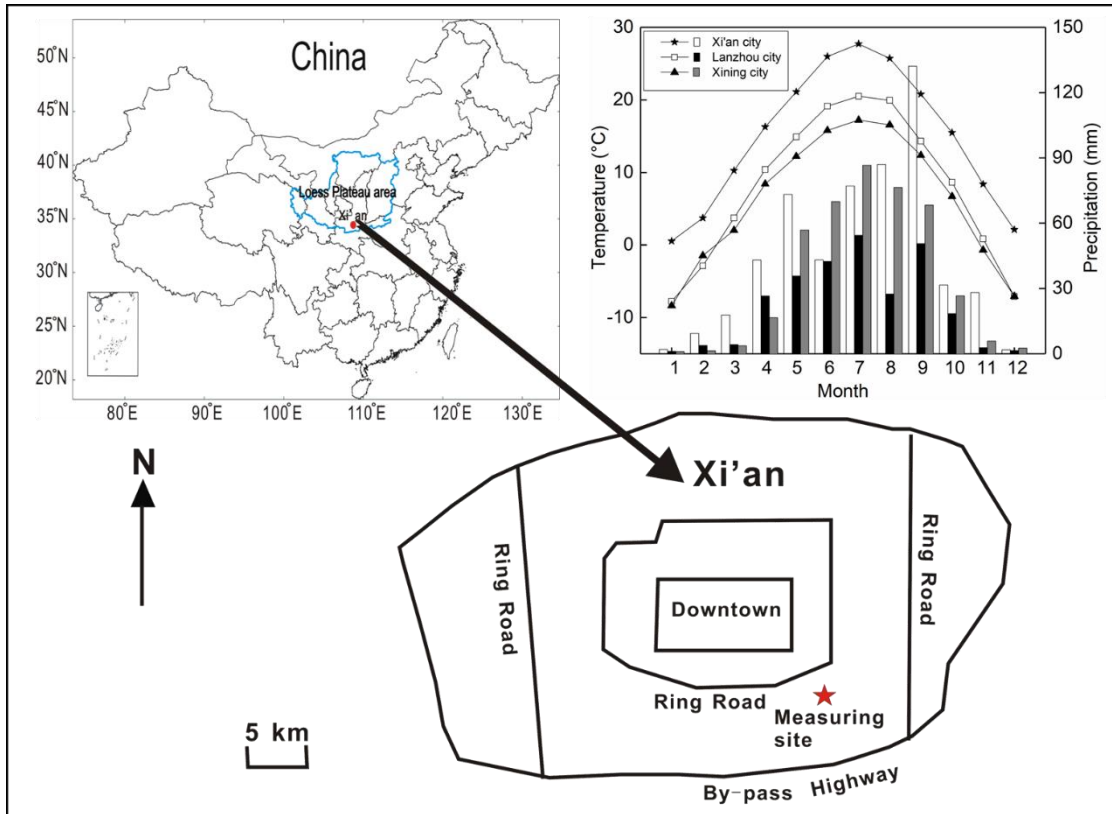
167

168 **2 Data and methods**

169 **2.1 Sampling site**

170 As the capital city of Shaanxi Province and the largest city in Northwest China, Xi'an
171 is located on the Guanzhong Plain on the southern edge of the CLP at an average
172 elevation of 400 m. The city is located in a semiarid to arid region and is representative
173 of most cities in northern and northwestern of China (e.g., Lanzhou and Xining cities,
174 Fig. 1). The mean annual precipitation is 573.7 mm, and the mean annual evaporation
175 is 426.6 mm from 1951 to 2008 (Wu et al., 2013). The notable below-cloud evaporation

176 effect has been reported in many studies for this area (Sun et al., 2020; Wan et al.,
 177 2018; Zhu et al., 2016). Therefore, it is an ideal site to study below-cloud processes.



178 Figure 1. Average monthly variations in temperature and precipitation in Xi'an, Lanzhou, and
 179 Xining during 2010-2015. Location of the sampling site in the Yanta Zone, 9 km SE of downtown
 180 Xi'an. Water vapor samples are taken on the seventh floor of a twelve-story building,
 181 approximately 30 m above ground level. Precipitation samples are collected on the top floor, 1
 182 m above ground level.

183

184 The water vapor in situ measurement site is located in a residential area, approximately
 185 10 km southeast of downtown Xi'an city (Fig. 1). The atmospheric water vapor isotopic
 186 composition was observed from 1 January 2016 to 31 December 2017 on the seventh
 187 floor of the Institute of Earth and Environment, Chinese Academy of Sciences,
 188 approximately 30 m above ground. The rainfall or snowfall collector was placed on the
 189 rooftop of the buildings (1 m above the floor of the roof), approximately 50 m above
 190 ground.

191

192 2.2 Sampling and isotopic measurement

193 Rainfall and snowfall samples were collected manually from the beginning of each
 194 precipitation event using a polyethylene collector (700 × 450 × 170 mm). Before being
 195 used, the collector was cleaned with soap and water, rinsed with deionized water, and
 196 then dried. When the precipitation event ended, the collector was quickly taken back

197 to minimize water evaporation. The rainfall volume was measured using a graduated
198 flask. After collection, the samples were filtered through 0.40- μm polycarbonate
199 membranes. Then, the rainfall samples were immediately poured into 100 ml
200 polyethylene bottles. The snowfall samples were first melted at room temperature in
201 closed plastic bags, second the samples were filtered, and then immediately poured
202 into 100 ml polyethylene bottles. Approximately 2 ml of each filtrate was transferred
203 into a sample vial and stored at -4 °C until analysis. Of the 141 collected samples,
204 during the two-year sampling campaigns, 130 were rainfall samples, and the other 11
205 were snowfall samples (Table S3).

206

207 In all cases, the data are reported in the standard delta notation (δ), i.e., the per mil
208 (‰) deviation from Vienna Standard Mean Ocean Water according to, $\delta =$
209 $(R_{\text{sample}}/R_{\text{reference}}-1) \times 1000$, where R is the isotope ratio of the heavy and light isotopes
210 (e.g., $^{18}\text{O}/^{16}\text{O}$) in the sample and the reference.

211

212 The precipitation samples were analyzed with a Picarro L2130-i (serial number HIDS
213 2104) wavelength-scanned cavity ring-down spectrometer in high-precision mode.
214 Every isotopic standard or sample was injected sequentially 8 times using a 5 μL
215 syringe, and then the arithmetic average of the last 3 injections was accepted as the
216 final result. All the samples were calibrated by three laboratory standards, while the
217 $\delta^{18}\text{O}$ and $\delta^2\text{H}$ true values of the three laboratory standards (Laboratory Standard-1
218 (LS-1): $\delta^{18}\text{O} = +0.3\text{‰}$, $\delta^2\text{H} = -0.4\text{‰}$; Laboratory Standard-2 (LS-2): $\delta^{18}\text{O} = -8.8\text{‰}$, $\delta^2\text{H}$
219 $= -64.8\text{‰}$; Laboratory Standard-3 (LS-3): $\delta^{18}\text{O} = -24.5\text{‰}$, $\delta^2\text{H} = -189.1\text{‰}$) are
220 calibrated to the scale of two international standards VSMOW-GISP (Vienna Standard
221 Mean Ocean Water –Greenland Ice Sheet Precipitation), with a precision of $\pm 0.2\text{‰}$
222 and $\pm 1.0\text{‰}$ for $\delta^{18}\text{O}$ and $\delta^2\text{H}$, respectively. To correct the instrument drift, the
223 instrument was repeatedly calibrated with the laboratory standards after analyzing 8
224 samples.

225

226 Atmospheric water vapor $\delta^{18}\text{O}_v$ and $\delta^2\text{H}_v$ were also analyzed by Picarro L2130-i but in
227 liquid-vapor dual mode. The inlet of the gas-phase instrument is connected to the vapor
228 source through an external solenoid valve when measuring vapor samples. This valve
229 can switch the input of the instrument from the vapor sample to dry gas. The instrument
230 is connected to dry gas prior to being connected to the evaporator for measuring liquid
231 water standards so that any traces of the water vapor sample are removed from the
232 measurement cell. The standards are injected into the evaporator with a CTC Analytics

233 autosampler, PAL HTC-xt (Leap Technologies, Carrboro, NC, USA), and measured by
234 the laser spectrometer. The atmospheric water vapor is pumped through a 2 m
235 stainless-steel tube (1/8 inch) using a diaphragm pump at a speed of 4 L min⁻¹ and
236 detected by the laser spectrometer. The outside length of the stainless-steel tube is
237 approximately 0.5 m, and the inside length is approximately 1.5 m. We covered the
238 stainless-steel tube with heating tape maintained at 60 °C to prevent water vapor from
239 condensing in the stainless-steel tube. The air intake was protected with a shield to
240 prevent rainwater from entering the sample line and direct sunlight.

241

242 The raw water vapor $\delta^{18}\text{O}_v$ and $\delta^2\text{H}_v$ data were obtained at approximately 1 Hz and
243 then block-averaged into 1 h intervals. As the main usage of this instrument is to
244 measure liquid water samples in our laboratory, it is used to monitor water vapor
245 isotopes in its spare time. Thus, the missing data indicate that the instrument is used
246 for measuring liquid samples or being maintained. The event-based water vapor
247 isotopic result is the average value from the start of the precipitation event to the end.

248

249 The hourly meteorological data, such as temperature, relative humidity (RH), and
250 surface pressure in Xi'an, are reported by the Chinese meteorological administration,
251 and can be downloaded from the website of <http://www.weather.com.cn/>. The
252 meteorological station is approximately 10 km to the north of our sampling site.

253

254 **2.3 The representativeness of data**

255 Over 2 years, a total of 514 days of water vapor isotopic composition measurements
256 were carried out. For 141 precipitation samples, 100 precipitation samples have
257 corresponding event-based water vapor isotopic results. In this study, the precipitation
258 events mainly occurred in summer and autumn and less frequently in winter and spring.
259 In summer and autumn, the rainfall amount accounted for more than 70% of the annual
260 rainfall (Fig. S3). This is consistent with the multiyear average precipitation distribution
261 in Xi'an (Fig. 1). Therefore, the collected samples are able to represent the precipitation
262 characteristics in this region.

263

264 **2.4 Water vapor isotopic data correction**

265 The water vapor concentration effect and isotopic composition dependency of the
266 cavity ringdown spectrometer have been pointed out by many studies (e.g., Bastrikov
267 et al., 2014; Benetti et al., 2014; Steen-Larsen et al., 2013; Weng et al., 2020). To
268 minimize the uncertainty from the measurement, it is important to determine the

269 isotopic composition-humidity correction response function. The humidity dependency
 270 shown in Fig. S1 also shows a dependency on the isotopic composition of the
 271 standards as reported by Weng et al. (2020). For example, in Fig. S1a and Fig. S1b,
 272 LS-1 shows a decrease in $\Delta\delta^{18}\text{O}$ and $\Delta\delta^2\text{H}$ with decreasing humidity, while LS-3 shows
 273 an increase with decreasing humidity. Therefore, we referred to Weng et al.'s (2020)
 274 correction scheme for the isotope composition-humidity dependency.

275

276 The isotopic measurements of ground-level $\delta^{18}\text{O}_v$ and $\delta^2\text{H}_v$ were corrected for isotopic
 277 composition-humidity dependency using the following:

$$278 \quad \Delta\delta_{\text{corr}} = \delta_{\text{meas}} - \delta_{\text{iso-hum-cor}} = \frac{a(\delta_{\text{iso-hum-cor}})}{h} + b(\delta_{\text{iso-hum-cor}}) \times h + c(\delta_{\text{iso-hum-cor}}) \quad (\text{Eq. 1})$$

279 where $\delta_{\text{iso-hum-cor}}$ is the isotopic composition-humidity dependency corrected water
 280 vapor isotopic composition at 20000 ppmv; δ_{meas} is the raw, measured isotopic
 281 composition at that humidity; h is the measured humidity; and a , b , and c are fitting
 282 coefficients for each water standard and isotope species. The detailed correction
 283 processes are provided in the supplementary material (Appendix A).

284

285 To calibrate the water vapor isotopic composition to the VSMOW-GISP scale, three
 286 known-value laboratory standards were used in the conversion, while these standards
 287 were analyzed in 24 h intervals to correct for instrument drift. The 1σ estimated total
 288 uncertainties are from 2.1 to 12.4 ‰ for $\delta^2\text{H}_v$, 0.4 to 1.7 ‰ for $\delta^{18}\text{O}_v$, and 3.8 to 18.4 ‰
 289 for $d\text{-excess}_v$ over the range of humidity from 30000 to 3000 ppmv on a 10-minute
 290 average through the approach using a Monte Carlo method.

291

292 **2.5 Analytical methods**

293 **2.5.1 $\Delta d\Delta\delta$ -diagram**

294 When raindrop falls from cloud base to ground, it continuously exchanges with
 295 surrounding vapor and may encounter net loss due to evaporation. However, this
 296 process is difficult to quantify by observation. Making use of stable water isotopes, Graf
 297 et al. (2019) introduced the $\Delta d\Delta\delta$ -diagram to diagnose the below-cloud processes and
 298 their effects on vapor and precipitation isotopic composition, since equilibration and
 299 evaporation are two different processes and lead to different directions in the two-
 300 dimensional phase space of the $\Delta d\Delta\delta$ -diagram. Here, the differences in the isotopic
 301 composition of precipitation-equilibrated vapor relative to the observed ground-level
 302 vapor can be expressed as:

$$303 \quad \Delta\delta_v = \delta_{\text{pv-eq}} - \delta_{\text{gr-v}} \quad (\text{Eq. 2})$$

304
$$\Delta d\text{-excess}_v = d\text{-excess}_{pv\text{-eq}} - d\text{-excess}_{gr\text{-v}} \quad (\text{Eq. 3})$$

305 where $\delta_{pv\text{-eq}}$ and $\delta_{gr\text{-v}}$ are the $\delta^2\text{H}$ ($\delta^{18}\text{O}$) of equilibrium vapor from precipitation and
 306 observed vapor near the ground, respectively, and $d\text{-excess}_{pv\text{-eq}}$ and $d\text{-excess}_{gr\text{-v}}$ are
 307 $d\text{-excess}$ values of the equilibrium vapor from precipitation and observed vapor near
 308 the ground, respectively. For the detailed calculation processes, please refer to the
 309 supplemental material (Appendix B) or Graf et al. (2019).

310

311 **2.5.2 Below-cloud evaporation calculation: Method 1**

312 As reported by Stewart (1975), the isotopic ratio of a falling water drop is:

313
$${}^iR_{gr} = {}^i\gamma {}^iR_{va} + ({}^iR_{cb} - {}^i\gamma {}^iR_{va})F_r{}^i\beta \quad (\text{Eq. 4})$$

314 where ${}^iR_{gr}$ is the isotopic ratio of falling raindrops near the ground; ${}^iR_{va}$ and ${}^iR_{cb}$ are the
 315 initial isotopic ratios for the vapor and raindrop at the cloud base; ${}^i\gamma$ and ${}^i\beta$ are the
 316 parameters related to the equilibrium fractionation factor, relative humidity, and
 317 molecular diffusivities; and F_r is the remaining fraction of raindrop mass after
 318 evaporation.

319

320 Assuming that the initial isotopic composition of the raindrop at the cloud base is in
 321 equilibrium with the surrounding water vapor, Froehlich et al. (2008) adapted the
 322 Stewart model and simplified the equation to evaluate the isotopic enrichment due to
 323 below-cloud evaporation by:

324
$$\Delta\delta_p = (1 - \frac{\gamma}{\alpha})(F_r^\beta - 1) \quad (\text{Eq. 5})$$

325
$$F_i = (1 - F_r) \times 100\% \quad (\text{Eq. 6})$$

326 where α is the equilibrium fractionation factor for hydrogen and oxygen isotopes; the
 327 parameters of γ and β are defined by Stewart (1975); F_r is the remaining fraction of
 328 raindrop mass after evaporation; $\Delta\delta_p$ is the raindrop isotopic variation due to below-
 329 cloud evaporation; and F_i is the evaporation proportion. For the detailed calculation
 330 processes, please refer to the supplemental material (Appendix C) or Froehlich et al.
 331 (2008), Wang et al. (2016b), and Salamalikis (2016).

332

333 **2.5.3 Below-cloud evaporation calculation: Method 2**

334 Because the isotopic composition of raindrop is directly influenced by the below-cloud
 335 processes during its falling, the below-cloud effects could be directly represented by
 336 the difference between the isotopic composition of precipitation at the ground level and
 337 cloud base:

338
$$\Delta\delta_p = \delta_{gr\text{-p}} - \delta_{cb\text{-p}} \quad (\text{Eq. 7})$$

339 where δ_{gr-p} and δ_{cb-p} are the isotopic compositions of a falling raindrop near the ground
340 and below the cloud base, respectively, and $\Delta\delta_p$ is the raindrop isotopic variation due
341 to below-cloud evaporation. δ_{gr-p} is our observed precipitation isotopic composition,
342 and δ_{cb-p} can be calculated by ground-level water vapor isotopic composition according
343 to Deshpande et al. (2010). For the detailed calculation processes, please refer to the
344 supplemental material (Appendix D) or Araguás-Araguás et al. (2000), Deshpande et
345 al. (2010), and Salamalikis (2016).

346

347 Here, it should be noted that both methods use an important assumption, which is that
348 the surface water vapor is (moist) adiabatically connected to the cloud-base water
349 vapor. In method 1, this assumption is used to calculate the cloud base height,
350 temperature, and pressure (Appendix C, Eq. 14-16). In method 2, the isotopic
351 composition of the cloud-base water vapor is calculated assuming a moist adiabatic
352 ascent of the measured ground-level water vapor (Appendix C, Eq. 22). In addition, in
353 method 2, we assume that the raindrop isotopic composition (δ_{cb-p}) at the cloud base
354 is in equilibrium with the surrounding water vapor, and the observed ground-level
355 precipitation isotopic composition (δ_{gr-p}) includes the processes of evaporation, growth,
356 and isotopic equilibrium with the surrounding vapor. Furthermore, the air column is
357 assumed to have no horizontal advection into or out of it and no updraft or downdraft
358 of the air masses during the hydrometeors' falling. That means the vertical column at
359 the observation site is undisturbed by horizontal movement. These assumptions only
360 hold if a single vertical column extends from the ground to the cloud-base height. If the
361 vertical column is affected by lateral entrainment of surrounding air, these assumptions
362 become invalid. The equilibrium exchange process is not separated from evaporation;
363 therefore, the $\Delta\delta$ results may underestimate the below-cloud evaporation effect in
364 method 2. To obtain accurate results, more work is needed to separate equilibration
365 process from the evaporation in future.

366

367 Actually, method 1 makes use of the mass change of the falling raindrop to evaluate
368 the below-cloud evaporation effect on isotopic composition, while method 2 evaluates
369 its effect by directly measuring the variations in isotope composition.

370

371 **2.5.4 Statistical Analysis**

372 To compare the difference between the two methods, the independent t test was
373 performed on Statistical Package for Social Sciences (SPSS 13.0, Inc., Chicago, US),
374 followed by setting the significant difference at the $p=0.05$ level of confidence.

375

376 3 Results and discussion

377 3.1 Relationship between water vapor and precipitation isotopic compositions

378 Influenced by below-cloud evaporation, the slope of the local meteoric water line (LMWL)

379 (LMWL) would be lower than 8, the precipitation isotopic composition would become

380 more positive, the d-excess of precipitation would be less than 10, and the equilibrated

381 water vapor isotopic composition would be more positive than the observed one. As

382 shown in Fig. 2, the LMWL is defined as $\delta^2H_p=7.0\times\delta^{18}O_p+3.0$ based on the event

383 precipitation isotopic composition, and the local water vapor line (LWVL) is defined as

384 $\delta^2H_v=7.8\times\delta^{18}O_v+15.1$ based on the per-precipitation-event water vapor isotopic

385 composition. Both the slope and intercept of the LMWL are lower than the global

386 meteoric water line (GMWL), which has a slope of 8.0 and intercept of 10.0 (Dansgaard,

387 1964; Gat, 1996), indicating the potentially significant below-cloud evaporation effect

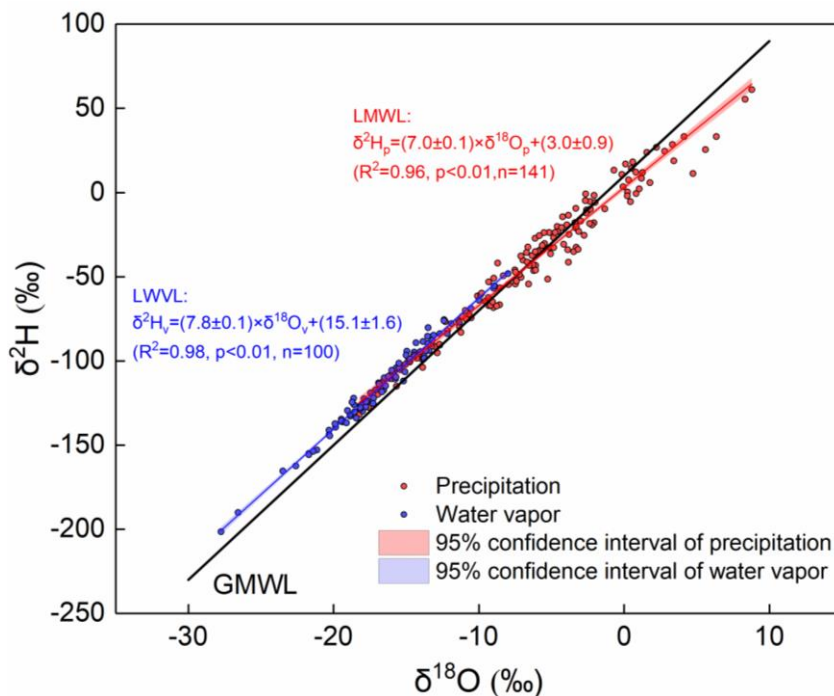
388 on precipitation (Froehlich et al., 2008). In general, the slopes of the meteoric water

389 lines are indicative of kinetic processes superimposed on the equilibrium fractionation,

390 and the somewhat lower slope of the LWVL (slope=7.8) than the expected equilibrium

391 fractionation (slope=8.0) may also be related to the increasing influence of kinetic

392 processes (Rangarajan et al., 2017).



393 Figure 2. Local meteoric water line (LMWL) and local water vapor line (LMVL) in Xi'an city.

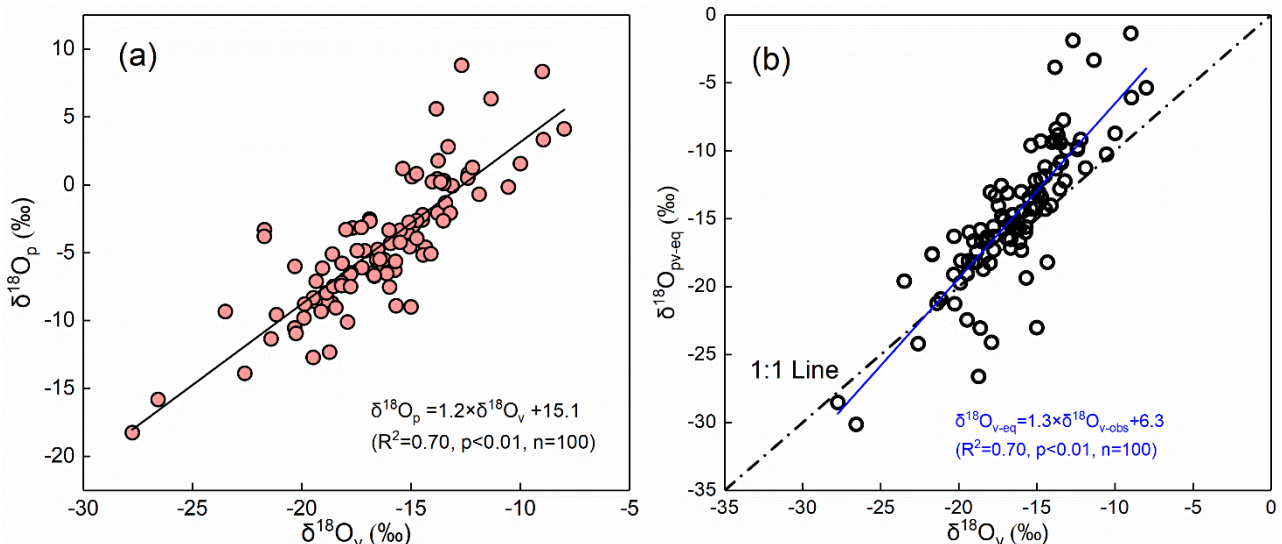
394

395 In addition, we noted that the water vapor and precipitation isotopic compositions were

396 basically distributed in different ranges, with the former being generally more negative

397 than the latter (Fig. 2). According to the classic isotopic fractionation theory, heavier
 398 isotopes preferentially condense into the liquid phase during the precipitation process,
 399 which results in the precipitation isotopic composition being more positive than the
 400 water vapor isotopic composition (Dansgaard, 1964). Hence, the distribution
 401 characteristics of water vapor and precipitation on the $\delta^{18}\text{O}$ - $\delta^2\text{H}$ plot would make us
 402 suppose that their isotopic compositions are in or close to equilibrium at this study site.
 403 To validate our assumption, we plot their relationship in Fig. 3a. As expected, they
 404 show a significant positive correlation ($R^2=0.70$, $p<0.01$), and thus, the water vapor
 405 isotopic composition can explain 70% of the variation in the precipitation isotopic
 406 composition. Furthermore, we used the measured precipitation isotopic composition to
 407 deduce the water vapor isotopic composition at the ground level according to the liquid-
 408 vapor equilibrium isotope fractionation ($\delta^{18}\text{O}_{\text{pv-eq}}$) and compared it with the observed
 409 water vapor ($\delta^{18}\text{O}_v$) in Fig. 3b. The scatterplot of the observed $\delta^{18}\text{O}_v$ against the
 410 equilibrated $\delta^{18}\text{O}_{\text{pv-eq}}$ also presents a significantly positive relationship (Fig. 3b).

411



412 Figure 3. Relationship between $\delta^{18}\text{O}_p$ of precipitation and $\delta^{18}\text{O}_v$ of water vapor in Xian (a); and
 413 the relationship between the equilibrium computed $\delta^{18}\text{O}_{\text{pv-eq}}$ based on the precipitation isotopic
 414 composition and the near ground observed $\delta^{18}\text{O}_v$ (b). The dashed-dotted line in (b) represents
 415 for the 1:1 line, and the blue line represents the regression line of the data.

416

417 In Fig. 3b, we also noted that the equilibrated $\delta^{18}\text{O}_{\text{pv-eq}}$ is relatively more positive than
 418 the observed $\delta^{18}\text{O}_v$. Because Xi'an city belongs to a semiarid area, raindrops are likely
 419 to evaporate in an unsaturated environment during falling. Therefore, the positive
 420 $\delta^{18}\text{O}_{\text{pv-eq}}$ is caused by the non-equilibrium fractionation in low relative humidity, which
 421 makes the $\delta^{18}\text{O}_{\text{pv-eq}}-\delta^{18}\text{O}_v$ points deviate from the 1:1 line.

422

423 The reasonable agreement of observed and equilibrated water vapor isotopic
424 compositions has been reported by Jacob and Sonntag (1991), Welp et al. (2008), and
425 Wen et al. (2010); however, they postulated the different relationships underlying $\delta^{18}\text{O}_v$
426 and $\delta^{18}\text{O}_{\text{pv-eq}}$. Jacob and Sonntag (1991) suggested that the water vapor isotopic
427 composition can be deduced from the corresponding precipitation isotopic composition,
428 but Wen et al. (2010) speculated that the equilibrium method cannot accurately predict
429 the ground-level water vapor isotopic composition in arid and semiarid climates
430 because the monthly equilibrated water vapor values in April and November deviate
431 from the observed values. Here, with two years of continuous observations, the mean
432 difference between $\delta^{18}\text{O}_v$ and $\delta^{18}\text{O}_{\text{pv-eq}}$ is -1.1‰ for $\delta^{18}\text{O}$, -8.1‰ for $\delta^2\text{H}$, and 0.7‰ for
433 d-excess. Although there is a good relationship between $\delta^{18}\text{O}_v$ and $\delta^{18}\text{O}_{\text{pv-eq}}$ in our data,
434 below-cloud evaporation has a significant influence on the precipitation isotopic
435 composition. Therefore, cautious should be taken when deriving the water vapor
436 isotopic composition from the precipitation isotopic composition.

437

438 **3.2 Below-cloud processes indicated by the $\Delta d\Delta\delta$ -diagram**

439 Traditionally, to qualitatively assess the below-cloud evaporation of raindrops, the
440 value of $d\text{-excess}_p$ is a benchmark. Due to the differences in diffusivities of the
441 individual water molecules in non-equilibrium fractionation, $d\text{-excess}_p$ will deviate from
442 0‰ , which is a theoretical value under vapor-liquid equilibrium fractionation at
443 temperatures of approximately 20 °C (Gat, 1996). The global mean value of 10‰ for
444 the $d\text{-excess}_p$ in precipitation indicates that evaporation is in general a non-equilibrium
445 process. Normally, below-cloud evaporation will decrease $d\text{-excess}_p$, and in
446 comparison, mixing with the recycled water vapor from surface evaporation and plant
447 transpiration will increase $d\text{-excess}_p$ (Craig, 1961; Dansgaard, 1964). In addition, in
448 the water molecule diffusion process, the water vapor $d\text{-excess}_v$ may be modified,
449 which enhances the uncertainty in gauging the below-cloud evaporation process by
450 solely using $d\text{-excess}_p$. In contrast, the $\Delta d\Delta\delta$ -diagram introduced by Graf et al. (2019)
451 provides more information on below-cloud processes.

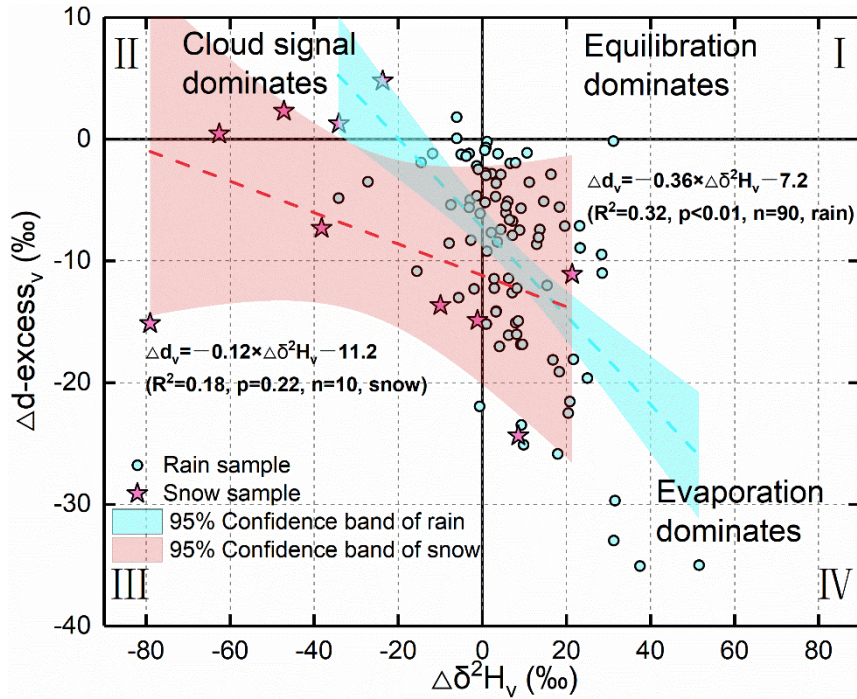
452

453 Theoretically, on the $\Delta d\Delta\delta$ -diagram, $\Delta d < 0\text{‰}$ and $\Delta\delta > 0\text{‰}$ indicate the below-cloud
454 evaporation process; $\Delta\delta < 0\text{‰}$ represents that the falling raindrop is less influenced by
455 below-cloud evaporation and retains the cloud signals; and Δd and $\Delta\delta$ close to 0‰
456 suggest equilibrium conditions. By projecting our data on the $\Delta d\Delta\delta$ -diagram, the
457 evaporation, equilibration, and nonexchange (e.g., a snowfall event or a transition from
458 rain to snow with a stronger cloud signal) processes could be clearly differentiated. It

459 is apparent in Fig. 4 that most of the rainfall samples are located in the fourth quadrant
460 with positive $\Delta\delta^2H_v$ and negative $\Delta d\text{-excess}_v$, indicating that evaporation is the major
461 below-cloud process. Interestingly, most of the snowfall samples seize the second and
462 third quadrants with negative $\Delta\delta^2H_v$, which is suggestive of below-cloud evaporation
463 with less impact on them, and their initial signals are well retained after cloud-based
464 equilibrium fractionation.

465

466 Based on the results from numerical simulations and in situ observations, Graf et al.
467 (2019) concluded that raindrop size and precipitation intensity are two important
468 factors for determining below-cloud processes. For example, precipitation with large
469 raindrops and heavy intensities is less affected by below-cloud processes because of
470 the shorter residence time of raindrops in the atmospheric column with a faster fall
471 velocity. Therefore, they are less affected by the evaporation and equilibration
472 processes on their falling way toward the ground, and the $\Delta\delta^2H_v$ is more negative. It is
473 worth noting that in the case of not considering the factors of raindrop size and rain
474 rate, the different precipitation types also show a clear distribution on the $\Delta d\Delta\delta$ -
475 diagram, as almost all the snowfall samples have negative $\Delta\delta^2H_v$ values (Fig. 4).
476 Theoretically, snowfall events normally occur in low-temperature conditions and
477 correspond to weak evaporation. Furthermore, the diffusion speed of the ice phase
478 (solid) to vapor is lower than that of liquid to vapor. Hence, under such conditions, the
479 isotopic signals of hydrometeor are less affected by the below-cloud processes during
480 falling. This leads $\Delta\delta$ to be more negative with decreasing temperature, such as the
481 observed phenomenon in the post-frontal precipitation isotopes in Graf et al.'s (2019)
482 study. Additionally, on the $\Delta d\Delta\delta$ -diagram, the snow samples with positive $\Delta d\text{-excess}_v$
483 (in the second quadrant) may be related to the supersaturation process, as the water
484 has unusually high $d\text{-excess}_p$ for the non-equilibrium fractionation of supersaturation
485 (Deshpande et al., 2013; Jouzel and Merlivat, 1984). We conclude that in addition to
486 raindrop size and rain rate, precipitation type is also an essential factor in determining
487 the data distributions on the $\Delta d\Delta\delta$ -diagram.



488 Figure 4. The projection of our data on the suggested $\Delta d\Delta\delta$ -diagram by Graf et al. (2019). The
 489 solid lines represent Δd -excess_v and $\Delta\delta^2H_v$ of 0‰. The dashed line corresponds to the linear
 490 fit through the samples with the 95% confidence band in shading. The red line is for rainfall
 491 samples, and the cyan line is for snowfall samples. The Roman numerals represent the
 492 category of the quadrant.

493

494 In Fig. 4, the slope of $\Delta d/\Delta\delta$ is -0.36 for the rainfall samples and -0.12 for the snowfall
 495 samples. Graf et al.'s (2019) reported a $\Delta d/\Delta\delta$ slope of -0.3. It should be noted that the
 496 slope of Graf et al. (2019) is based on intra-event samples (from the start to the end of
 497 precipitation, each interval of 10 min to collect one sample), while ours is based on
 498 per-event samples (only one sample was collected in each precipitation event).
 499 Although the time scale is different in the two studies, interestingly, the rainfall slopes
 500 are close to each other, while the snowfall slope is obviously different from the rainfall
 501 slope. The $\Delta d/\Delta\delta$ slope of -0.3 could represent a general characteristic of rainfall for
 502 continental mid-latitude cold front passages (Graf et al., 2019). Xi'an city is located
 503 near 35°N in inland China, which belongs to the continental mid-latitude region. In
 504 comparison, the $\Delta d/\Delta\delta$ slope of our snow samples is less negative. Therefore, the
 505 different $\Delta d/\Delta\delta$ slopes might be related to the different climatic characteristics or
 506 precipitation types. Certainly, to validate this assumption, more work needs to be done
 507 in future studies.

508

509 3.3 Comparing and analyzing the two methods

510 The $\Delta d\Delta\delta$ -diagram provides valuable information on the below-cloud processes, but
 511 it is only a qualitative analysis. In comparison, quantitative evaluation is more important

512 to identify the below-cloud evaporation effect. Here, we chose two methods to calculate
513 the variations in $\Delta\delta^2H_p$ and the evaporation fraction (F_i) on per-event precipitation and
514 compared their differences.

515

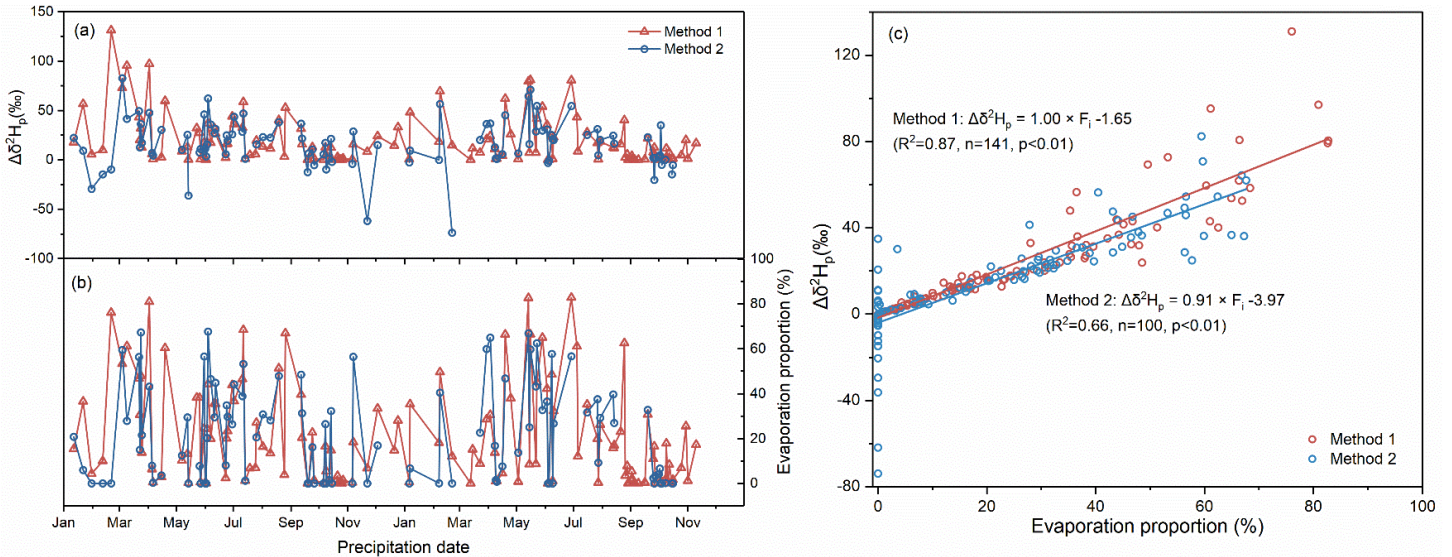
516 **3.3.1 Quantitative evaluation of the below-cloud evaporation derived from the** 517 **two methods**

518 The $\Delta\delta^2H_p$ ranges from 0 to 131.1 ‰ with an average and standard deviation of 17.8
519 ± 23.8 ‰, and the F_i ranges from 0 to 82.7% with an average and standard deviation
520 of 16.3 ± 21.9 % ($n=141$) for method 1. The $\Delta\delta^2H_p$ ranges from -73.8 to 82.5‰ with an
521 average and standard deviation of 16.3 ± 24.4 ‰, and the F_i ranges from 0 to 67.6%
522 with an average and standard deviation of 22.1 ± 21.7 % ($n=100$) for method 2. For the
523 90 rainfall events with corresponding water vapor data, the average and standard
524 deviation are 18.4 ± 21.7 ‰ for $\Delta\delta^2H_p$ derived from method 1, and the value is $18.7 \pm$
525 20.6 ‰ for $\Delta\delta^2H_p$ derived from method 2. For the 10 snowfall events, the average and
526 standard deviation of $\Delta\delta^2H_p$ are 42.6 ± 43.7 ‰ for method 1 and -6.1 ± 41.6 ‰ for
527 method 2. In the two methods, according to the independent t test, there are no
528 significant differences in the $\Delta\delta^2H_p$ of rainfall samples ($F=0$, $p=0.91$, $n=90$), but the
529 $\Delta\delta^2H_p$ of snowfall shows a large difference ($F=0.196$, $p<0.05$, $n=10$).

530

531 As shown in Fig. 5a and Fig. 5b, the $\Delta\delta^2H_p$ and F_i in the two methods have similar
532 fluctuation trends. A positive $\Delta\delta^2H_p$ and high F_i appear from March to July, while a
533 negative $\Delta\delta^2H_p$ and low F_i appear from September to following February. In addition,
534 the most positive $\Delta\delta^2H_p$ values are captured by method 1, while the most negative
535 values are detected by method 2. To analyze the underlying reason, we checked the
536 equation used to calculate $\Delta\delta^2H_p$. We noted that in Eq. 5, F_r is always lower than 1,
537 and thus $(F_r^\beta - 1)$ is negative. Similarly, $\frac{Y}{\alpha}$ is smaller than 1, and thus, $(1 - \frac{Y}{\alpha})$ is also
538 negative. Therefore, the $\Delta\delta^2H_p$ calculated by method 1 is always positive. In method 2,
539 the most negative $\Delta\delta^2H_p$ values are related to snowfall events. During the
540 supersaturation process, vapor deposition takes place over ice in the cloud (Jouzel
541 and Merlivat, 1984) with non-equilibrium fractionation (the kinetic fractionation factor
542 $\alpha_k < 1$), leading to the effective isotopic fractionation factor ($\alpha_{eff} = \alpha_{eq}\alpha_k$) being smaller
543 than the equilibrium fractionation coefficient (α_{eq}), and resulting in the ground-observed
544 δ_{gr-p} of solid precipitation (snow) being more depleted than the calculated δ_{cb-p} under
545 equilibrium fractionation (in Eq. 7). In fact, the mass of snow also increases under
546 supersaturation conditions; however, method 1 only considers the evaporation process.
547 The diameter of the raindrop used to determine the terminal velocity and evaporation

548 intensity (Supplemental material, Eqs. 10-13) does not take into account the different
 549 relationship of fall velocity to hydrometeor size for snowflakes and raindrops, which
 550 results in great uncertainty in method 1. Therefore, method 1 is not suitable for
 551 evaluating the below-cloud effect on the precipitation isotopic composition for snowfall
 552 or low-temperature rainfall events.



553 Figure 5. The variation in $\Delta\delta^2H_p$ for per-event precipitation in method 1 and method 2 (a); the
 554 same as (a) but for F_i (b); the relationship between F_i and $\Delta\delta^2H_p$ in method 1 and method 2 (c)

555

556 In addition, the influence of the below-cloud evaporation effect on δ^2H_p is heavier in
 557 method 1 than in method 2, especially at higher F_i conditions (Fig. 5c), because the
 558 slope of $F_i/\Delta\delta^2H$ in method 1 (1.00 ‰/‰) is slightly steeper than that in method 2
 559 (0.91 ‰/‰), and the intercept in method 1 (-1.65) is more positive than that in method
 560 2 (-3.97). Thus, under the same evaporation intensity, $\Delta\delta^2H_p$ is more enriched in
 561 method 1 than in method 2.

562

563 On the seasonal scale, both methods show that the below-cloud evaporation effect is
 564 heavier in spring and summer and weaker in autumn and winter (Fig. S4). Their
 565 differences are the smallest in spring and the largest in winter. The significant
 566 difference in winter might be related to the predominance of solid precipitation, which
 567 is not accounted for in method 1.

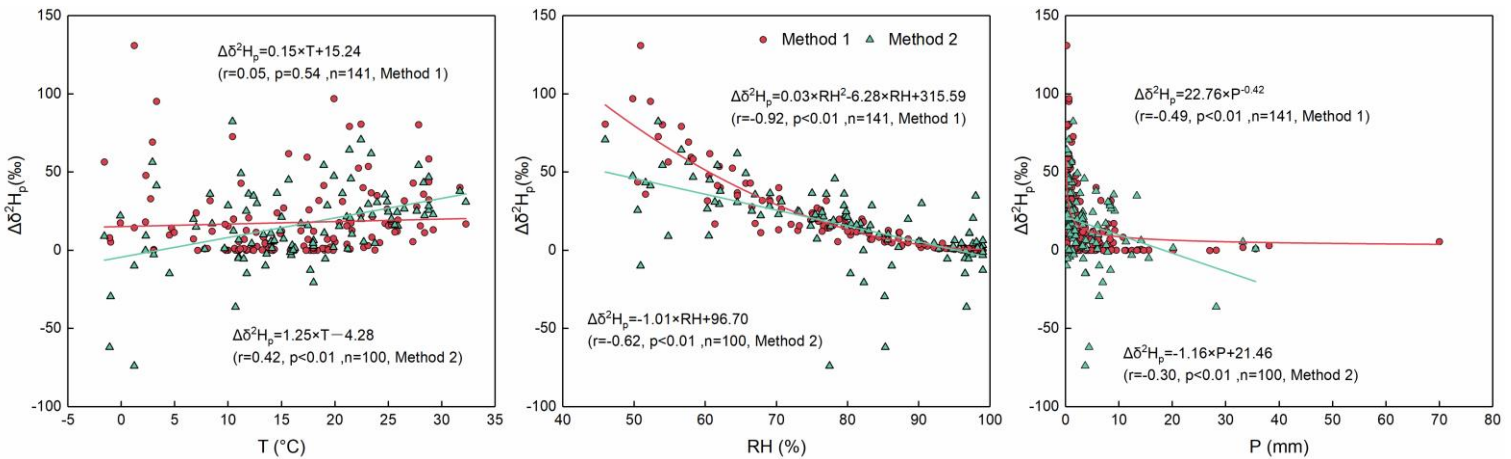
568

569 3.3.2 Meteorological controls on the two methods

570 To further explore the differences in the two methods, we performed correlation
 571 analyses between meteorological factors and $\Delta\delta^2H_p$ (Fig. 6). The results show that RH
 572 is the most important meteorological factor for both methods (Fig. 6b). Furthermore,
 573 the impact of RH on the variations in $\Delta\delta^2H_p$ is stronger in method 1 ($r=-0.92$) than in

574 method 2 ($r=-0.62$), and this phenomenon is more obvious when the RH is lower than
 575 60%. Although precipitation amounts have influences on both methods as well, their
 576 effect on $\Delta\delta^2H_p$ is rather weak ($r=-0.49$, method 1; $r=-0.30$, method 2; Fig. 6c), and the
 577 relationships are nonlinear. For temperature, in method 1, there is no clear correlation
 578 between $\Delta\delta^2H_p$ and temperature ($r=0.05$), and in method 2 their positive correlation is
 579 weak ($r=0.42$).

580



581 Figure 6. The correlations between $\Delta\delta^2H_p$ and the temperature in method 1 (red dots) and in
 582 method 2 (green triangles) (a); the same as (a) but for RH (b); the same as (a) and (b) but for
 583 precipitation amount (c).

584

585 In both methods, under an arid environment with high temperature, low RH, and small
 586 precipitation amounts, the evaporation effect on $\Delta\delta^2H_p$ is large. However, under the
 587 low-temperature conditions (below 5 °C), there is a divergence in $\Delta\delta^2H_p$ for the two
 588 methods, which is partly attributed to the supersaturation condition. With increasing
 589 RH, $\Delta\delta^2H_p$ becomes closer to 0 in both methods, but the variation in $\Delta\delta^2H_p$ is large in
 590 method 2 and very limited in method 1 when the RH is higher than 80%. There is a
 591 wide range, from 0 to 130‰, for $\Delta\delta^2H_p$ when the precipitation amount is small. As the
 592 precipitation amount is above 10 mm, the value of $\Delta\delta^2H_p$ tends toward 0‰.

593

594 3.3.2 Sensitivity test

595 In method 1, the input physical parameters include temperature, RH, precipitation
 596 amount, and surface pressure. In method 2, the same input parameters as for method
 597 1 were used except for the precipitation amount. Therefore, these parameters are
 598 considered in the sensitivity tests.

599

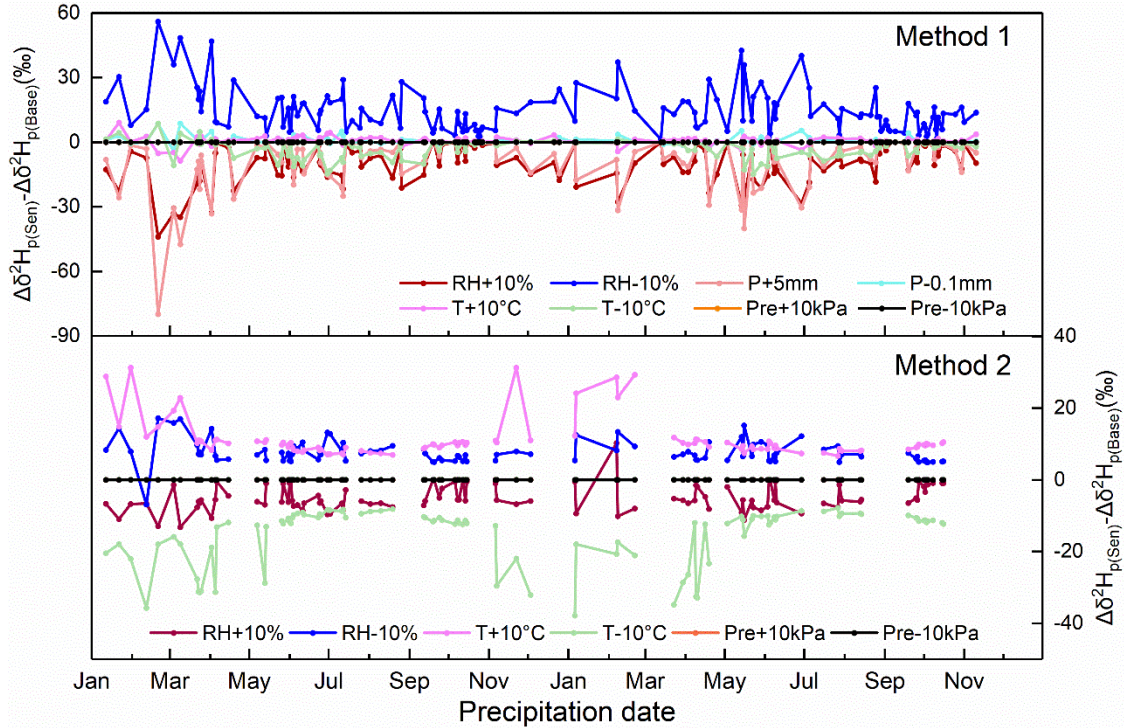
600 For the RH test, one case adds 10% to the measured RH, and another case subtracts
 601 10% from the measured RH. If the RH values are above 100%, then they are artificially

602 set to 99% to conform to reality. Two temperature scenarios, plus and minus 10 °C
603 based on the actual temperature, are analyzed. In the sensitivity test of precipitation
604 amount, considering that the amounts are lower than 0.1 mm in some precipitation
605 events, the reduction lower limit is set to 0.1 mm, and the enhancement upper limit is
606 set to 5 mm. On the basic surface pressure condition, a 10 kPa pressure fluctuation is
607 considered for its impact.

608

609 As shown in Fig. 7, the increase in RH and precipitation, and decrease in temperature
610 have a negative impact; that is, the below-cloud evaporation effect on the isotopic
611 composition will be attenuated. In contrast, the decrease in RH and precipitation and
612 increase in temperature have a positive impact, indicating that the below-cloud
613 evaporation effect will be strengthened. The varying surface pressure has no impact
614 on $\Delta\delta^2H_p$ for both methods. Moreover, the influencing strength of the different physical
615 parameters on $\Delta\delta^2H_p$ is different in the two methods. For example, in method 1, the
616 increase in temperature basically does not change the evaporation effect on $\Delta\delta^2H_p$,
617 and the influence of decreasing temperature on mitigating evaporation is limited as
618 well. However, the situation is totally different in method 2, where the temperature is a
619 decisive factor. In addition, the influence of RH is over the temperature in method 1,
620 but the condition is reversed in method 2. The precipitation amount is also an important
621 factor, as the influence of precipitation on $\Delta\delta^2H_p$ even surpasses the RH when it is
622 increased by 5 mm. Because of the limited decrease in precipitation amount, its
623 positive feedback is difficult to evaluate.

624



625 Figure 7. Sensitivity test of $\Delta\delta^2H_p$ under different cases. In method 1, the cases include $\pm 10\%$
 626 RH, $\pm 10^\circ\text{C}$ temperature, $\pm 10\text{ kPa}$ surface pressure, $+5\text{ mm}$ precipitation amount, and -0.1
 627 mm precipitation amount. In method 2, the cases include $\pm 10\%$ RH, $\pm 10^\circ\text{C}$ temperature, and
 628 $\pm 10\text{ kPa}$ surface pressure. $\Delta\delta^2H_{p(\text{Sen})}$ represents the results of the sensitivity test, and
 629 $\Delta\delta^2H_{p(\text{Base})}$ represents the results of the base condition.
 630

631 In the calculation process of method 2 (Eq. 7, and supplemental material, Eq. 22),
 632 except for the measured ground-level precipitation and water vapor isotopic
 633 compositions ($\delta_{\text{gr-p}}$ and $\delta_{\text{gr-v}}$), the other two controlling factors are the equilibrium
 634 fractionation factor (α) and the cloud base height. α is determined by the temperature
 635 variations of the cloud base, while the cloud base height is related to surface
 636 temperature and RH (supplemental material, Eq. 14-17). With increasing RH, the cloud
 637 base heights decrease, and vice versa (Fig. S5). In comparison, the cloud base heights
 638 are not sensitive to the changes in temperature (Fig. S5).
 639

640 Compared with method 2, the calculation process of method 1 is more complex. Many
 641 variables, such as raindrop diameter, evaporation intensity, raindrop falling velocity,
 642 and cloud base height, etc., need to be considered, while they are convoluted with
 643 temperature, RH, precipitation amount, and surface pressure. Through the sensitivity
 644 test, RH and precipitation amount are the two decisive factors in method 1 for
 645 determining the below-cloud evaporation intensity.
 646

647 3.3.2 Uncertainty estimations

648 There are many uncertainties in the two methods' estimates. In method 1, the input
649 parameters include the variation in temperature, RH, precipitation amount, and surface
650 pressure. In method 2, the uncertainty comes from the variations in the input
651 temperature, RH, surface pressure, ground level water vapor $\delta^2\text{H}_{\text{gr-v}}$, and precipitation
652 $\delta^2\text{H}_p$. However, the variations in surface pressure show no impact on $\Delta\delta^2\text{H}_p$ in the
653 sensitivity test; therefore, they are not considered in the uncertainty calculation.

654

655 To check the influence of temperature, RH, precipitation amount, and precipitation $\delta^2\text{H}_p$
656 on the below-cloud evaporation effect, we assume that the errors are mainly from the
657 measurement uncertainty of the instrument, which is $\pm 0.3\text{ }^\circ\text{C}$, $\pm 3\%$, $\pm 4\%$ precipitation
658 amount, and $\pm 1.0\text{‰}$, respectively. Due to the humidity effect (Sect. 2.4), the measured
659 $\delta^2\text{H}_{\text{gr-v}}$ for each event has a wide range of uncertainty, which varies from 1.3 to 8.2‰.
660 Hence, the lower and upper limits of the above used input parameters for method 1
661 and method 2 are used to quantify the uncertainties and add them quadratically to
662 ascertain the total uncertainty (Rangarajan et al., 2017; Wu et al., 2022). We obtain
663 the overall uncertainty varying from 0.71 to 0.72‰ for method 1, and from 0.60 to 1.05‰
664 for method 2 in the estimates of $\Delta\delta^2\text{H}_p$ values (refer to supplemental material,
665 Appendix E).

666

667

668 **4 Conclusions**

669 The below-cloud processes of precipitation are complex, variable, and influenced by
670 many factors, especially in arid and semiarid regions. Previously, below-cloud
671 evaporation was the most well-studied post-condensation process with the aid of the
672 slope of LMWL and d-excess of precipitation. In comparison, other below-cloud
673 processes, such as vapor-liquid equilibration or hydrometeor supersaturation growth,
674 have paid less attention to different rain types. In this study, based on the two years of
675 precipitation data collected in Xi'an, we compiled a set of methods to systematically
676 evaluate the below-cloud evaporation effect on the local precipitation isotopic
677 composition and obtained the following main conclusions:

678 1. In arid areas, the precipitation and water vapor isotopic compositions are closely
679 related, and thus the joint observation of the two tracers could provide more information
680 on precipitation processes. In Xi'an, the below-cloud evaporation effect is stronger in
681 spring and summer and weaker in autumn and winter and is related to the variation in
682 the local RH.

683 2. Our work evaluates the general applicability of the $\Delta d\Delta\delta$ -diagram. Although there is

684 a difference in timescale between Graf et al.'s (2019) study (intra-event) and ours (per-
685 event), the influence of below-cloud processes on our precipitation and water vapor
686 isotopic data can be clearly visualized on the $\Delta d/\Delta \delta$ -diagram. In this study, below-cloud
687 evaporation is the main process during raindrop fall. However, snowfall samples are
688 less influenced by evaporation, and mainly preserve their initial water vapor
689 information. The different $\Delta d/\Delta \delta$ slopes of rainfall and snowfall might be related to the
690 precipitation types.

691 3. By comparing the two methods, there are no significant differences in $\Delta \delta^2 H_p$ for
692 rainfall events, but they show a large difference for snowfall events, and this is related
693 to the supersaturation process not being considered in method 1. The slope of $F_i/\Delta \delta^2 H$
694 in method 1 (1.00 ‰/‰) is slightly steeper than that in method 2 (0.91 ‰/‰), indicating
695 a stronger evaporation effect on $\Delta \delta^2 H$ for method 1. Through meteorology and
696 sensitivities analysis, we found that in the two methods, RH is the main controlling
697 factor, and temperature shows different impacts on the variations in $\Delta \delta^2 H$. Through
698 uncertainty estimations, method 2 shows a larger uncertainty range (ranging from 0.60
699 to 1.05‰) than method 1 (ranging from 0.71 to 0.72‰).

700 4. Considering the assumption that the surface water vapor is (moist) adiabatically
701 connected to the cloud-base water vapor, the validation of the two methods is for
702 specific weather conditions, such as convective precipitation. Here, method 1 only
703 includes below-cloud evaporation by construction, while in method 2, other processes
704 can still be included, such as supersaturation. Therefore, both methods are suited to
705 study the below-cloud evaporation effect (no significant differences in $\Delta \delta^2 H_p$ for rainfall
706 events); however, if other below-cloud processes are included, applying method 2 is
707 the better choice. In future studies, further high-resolution observations of vertical
708 profiles of precipitation and water vapor isotopes, whether tower-based or aircraft-
709 based, have the potential to greatly improve constraints on below-cloud processes.

710

711

712 **Data availability**

713 The datasets can be obtained from Table S3.

714

715 **Author contribution**

716 Meng Xing and Weiguo Liu designed the experiments, interpreted the results, and
717 prepared the manuscript with contributions from all co-authors. Meng Xing and Jing
718 Hu analyzed the precipitation and water vapor samples. Jing Hu maintained the
719 experimental instruments.

720

721 **Competing interests**

722 The authors declare that they have no conflict of interest.

723

724

725 **Acknowledgment**

726 This work was supported by Science Foundation of China (No. 42177093), West Light
727 Foundation of The Chinese Academy of Sciences, and China scholarship council. The
728 authors would like to thank Mr. Xijing Cao for helping to collect precipitation samples.

729

730 **References**

731 Aemisegger, F., Sturm, P., Graf, P., Sodemann, H., Pfahl, S., Knohl, A. and Wernli, H.:
732 Measuring variations of δ 18O and δ 2H in atmospheric water vapour using two commercial
733 laser-based spectrometers: An instrument characterisation study, *Atmos. Meas. Tech.*, 5(7),
734 1491–1511, doi:10.5194/amt-5-1491-2012, 2012.

735 Araguás-Araguás, L., Froehlich, K. and Rozanski, K.: Deuterium and oxygen-18 isotope
736 composition of precipitation and atmospheric moisture, *Hydrol. Process.*, 14(8), 1341–1355,
737 doi:10.1002/1099-1085(20000615)14:8<1341::AID-HYP983>3.3.CO;2-Q, 2000.

738 Bastrikov, V., Steen-Larsen, H. C., Masson-Delmotte, V., Gribanov, K., Cattani, O., Jouzel, J.
739 and Zakharov, V.: Continuous measurements of atmospheric water vapour isotopes in western
740 Siberia (Kourovka), *Atmos. Meas. Tech.*, 7(6), 1763–1776, doi:10.5194/amt-7-1763-2014,
741 2014.

742 Benetti, M., Reverdin, G., Pierre, C., Merlivat, L., Risi, C., Steen-Larsen, H. C. and Vimeux, F.:
743 Deuterium excess in marine water vapor: Dependency on relative humidity and surface wind
744 speed during evaporation, *J. Geophys. Res.*, 119(2), 584–593, doi:10.1002/2013JD020535,
745 2014.

746 Bowen, G. J., Cai, Z., Fiorella, R. P. and Putman, A. L.: Isotopes in the Water Cycle: Regional-
747 to Global-Scale Patterns and Applications, *Annu. Rev. Earth Planet. Sci.*, 47(1), 453–479,
748 doi:10.1146/annurev-earth-053018-060220, 2019.

749 Cai, Y., Cheng, H., An, Z., Edwards, R. L., Wang, X., Tan, L. and Wang, J.: Large variations of
750 oxygen isotopes in precipitation over south-central Tibet during Marine Isotope Stage 5,
751 *Geology*, 38(3), 243–246, doi:10.1130/G30306.1, 2010.

752 Chakraborty, S., Sinha, N., Chattopadhyay, R., Sengupta, S., Mohan, P. M. and Datye, A.:
753 Atmospheric controls on the precipitation isotopes over the Andaman Islands, Bay of Bengal,
754 *Sci. Rep.*, 6, 19555 [online] Available from: <https://doi.org/10.1038/srep19555>, 2016.

755 Christner, E., Aemisegger, F., Pfahl, S., Werner, M., Cauquoin, A., Schneider, M., Hase, F.,
756 Barthlott, S. and Schädler, G.: The Climatological Impacts of Continental Surface Evaporation,
757 Rainout, and Subcloud Processes on δ D of Water Vapor and Precipitation in Europe, *J.*

758 Geophys. Res. Atmos., 123(8), 4390–4409, doi:10.1002/2017JD027260, 2018.

759 Clark, I. D. and Fritz, P.: *Environmental Isotopes in Hydrogeology*, Lewis, Boca Raton, Florida.,
760 1997.

761 Craig, H.: Isotopic Variations in Meteoric Waters, *Science* (80-.), 133(3465), 1702–1703, 1961.

762 Dansgaard, W.: Stable isotopes in precipitation, *Tellus*, 16(4), 436–468,
763 doi:10.3402/tellusa.v16i4.8993, 1964.

764 Deshpande, R. D., Maurya, A. S., Kumar, B., Sarkar, A. and Gupta, S. K.: Rain-vapor
765 interaction and vapor source identification using stable isotopes from semiarid western India, *J.*
766 *Geophys. Res. Atmos.*, 115(23), 1–11, doi:10.1029/2010JD014458, 2010.

767 Deshpande, R. D., Maurya, A. S., Kumar, B., Sarkar, A. and Gupta, S. K.: Kinetic fractionation
768 of water isotopes during liquid condensation under super-saturated condition, *Geochim.*
769 *Cosmochim. Acta*, 100, 60–72, doi:https://doi.org/10.1016/j.gca.2012.10.009, 2013.

770 Fiorella, R. P., Bares, R., Lin, J. C., Ehleringer, J. R. and Bowen, G. J.: Detection and variability
771 of combustion-derived vapor in an urban basin, *Atmos. Chem. Phys.*, 18(12), 8529–8547,
772 doi:10.5194/acp-18-8529-2018, 2018.

773 Fisher, D. A.: Remarks on the deuterium excess in precipitation in cold regions, *Tellus B*, 43(5),
774 401–407, doi:https://doi.org/10.1034/j.1600-0889.1991.t01-4-00006.x, 1991.

775 Froehlich, K., Kralik, M., Papesch, W., Rank, D., Scheifinger, H. and Stichler, W.: Deuterium
776 excess in precipitation of Alpine regions – moisture recycling, *Isotopes Environ. Health Stud.*,
777 44(1), 61–70, doi:10.1080/10256010801887208, 2008.

778 Gat, J. R.: OXYGEN AND HYDROGEN ISOTOPES IN THE HYDROLOGIC CYCLE, *Annu.*
779 *Rev. Earth Planet. Sci.*, 24(1), 225–262, doi:10.1146/annurev.earth.24.1.225, 1996.

780 Gorski, G., Strong, C., Good, S. P., Bares, R., Ehleringer, J. R. and Bowen, G. J.: Vapor
781 hydrogen and oxygen isotopes reflect water of combustion in the urban atmosphere, *Proc. Natl.*
782 *Acad. Sci.*, 112(11), 3247–3252, doi:10.1073/pnas.1424728112, 2015.

783 Graf, P., Wernli, H., Pfahl, S. and Sodemann, H.: A new interpretative framework for below-
784 cloud effects on stable water isotopes in vapour and rain, *Atmos. Chem. Phys.*, 19(2), 747–765,
785 doi:10.5194/acp-19-747-2019, 2019.

786 Guan, H., Zhang, X., Skrzypek, G., Sun, Z. and Xu, X.: Deuterium excess variations of rainfall
787 events in a coastal area of south Australia and its relationship with synoptic weather systems
788 and atmospheric moisture sources, *J. Geophys. Res. Atmos.*, 118(2), 1123–1138,
789 doi:10.1002/jgrd.50137, 2013.

790 Jacob, H. and Sonntag, C.: An 8-year record of the seasonal variation of 2 H and 18 O in
791 atmospheric water vapour and precipitation at Heidelberg, Germany, *Tellus B Chem. Phys.*
792 *Meteorol.*, 43(3), 291–300, doi:10.3402/tellusb.v43i3.15276, 1991.

793 Jeelani, G., Deshpande, R. D., Galkowski, M. and Rozanski, K.: Isotopic composition of daily
794 precipitation along the southern foothills of the Himalayas: Impact of marine and continental
795 sources of atmospheric moisture, *Atmos. Chem. Phys.*, 18(12), 8789–8805, doi:10.5194/acp-
796 18-8789-2018, 2018.

797 Jouzel, J. and Merlivat, L.: Deuterium and oxygen 18 in precipitation: Modeling of the isotopic

798 effects during snow formation, *J. Geophys. Res.*, 89(D7), 11749, doi:10.1029/jd089id07p11749,
799 1984.

800 Jouzel, J., Delaygue, G., Landais, A., Masson-Delmotte, V., Risi, C. and Vimeux, F.: Water
801 isotopes as tools to document oceanic sources of precipitation, *Water Resour. Res.*, 49(11),
802 7469–7486, doi:https://doi.org/10.1002/2013WR013508, 2013.

803 Li, L. and Garziona, C. N.: Spatial distribution and controlling factors of stable isotopes in
804 meteoric waters on the Tibetan Plateau : Implications for paleoelevation reconstruction, *Earth
805 Planet. Sci. Lett.*, 460, 302–314, doi:10.1016/j.epsl.2016.11.046, 2017.

806 Li, Z., Qi, F., Wang, Q. J., Kong, Y., Cheng, A., Song, Y., Li, Y., Li, J. and Guo, X.: Contributions
807 of local terrestrial evaporation and transpiration to precipitation using $\delta^{18}\text{O}$ and D-excess as
808 a proxy in Shiyang inland river basin in China, *Glob. Planet. Chang.*, 146, 140–151, 2016.

809 Liu, W., Feng, X., Liu, Y., Zhang, Q. and An, Z.: $\delta^{18}\text{O}$ values of tree rings as a proxy of monsoon
810 precipitation in arid Northwest China, *Chem. Geol.*, 206(1), 73–80,
811 doi:https://doi.org/10.1016/j.chemgeo.2004.01.010, 2004.

812 Liu, W., Liu, H., Wang, Z., An, Z. and Cao, Y.: Hydrogen isotopic compositions of long-chain
813 leaf wax n-alkanes in Lake Qinghai sediments record palaeohydrological variations during the
814 past 12 ka, *Quat. Int.*, 449, 67–74, doi:https://doi.org/10.1016/j.quaint.2017.05.024, 2017a.

815 Liu, W., Wang, H., Leng, Q., Liu, H., Zhang, H. and Xing, M.: Hydrogen isotopic compositions
816 along a precipitation gradient of Chinese Loess Plateau : Critical roles of precipitation /
817 evaporation and vegetation change as controls for leaf wax δD , *Chem. Geol.*, 528(April),
818 119278, doi:10.1016/j.chemgeo.2019.119278, 2019.

819 Liu, Y., Liu, H., Song, H., Li, Q., Burr, G. S., Wang, L. and Hu, S.: A monsoon-related 174-year
820 relative humidity record from tree-ring $\delta^{18}\text{O}$ in the Yaoshan region, eastern central China, *Sci.
821 Total Environ.*, 593–594, 523–534, doi:https://doi.org/10.1016/j.scitotenv.2017.03.198, 2017b.

822 Merlivat, L. and Jouzel, J.: Global climatic interpretation of the deuterium-oxygen 18 relationship
823 for precipitation, *J. Geophys. Res. Ocean.*, 84(C8), 5029–5033,
824 doi:https://doi.org/10.1029/JC084iC08p05029, 1979.

825 Peng, T. R., Liu, K. K., Wang, C. H. and Chuang, K. H.: A water isotope approach to assessing
826 moisture recycling in the island-based precipitation of Taiwan: A case study in the western
827 Pacific, *Water Resour. Res.*, 47(8), 1–11, doi:10.1029/2010WR009890, 2011.

828 Putman, A. L., Fiorella, R. P., Bowen, G. J. and Cai, Z.: A Global Perspective on Local Meteoric
829 Water Lines-SM, *Water Resour. Res.*, 1–6, doi:10.1351/pac198961081483.Jaffey, 2019a.

830 Putman, A. L., Fiorella, R. P., Bowen, G. J. and Cai, Z.: A Global Perspective on Local Meteoric
831 Water Lines: Meta-analytic Insight into Fundamental Controls and Practical Constraints, *Water
832 Resour. Res.*, 2019WR025181, doi:10.1029/2019WR025181, 2019b.

833 Rangarajan, R., Laskar, A. H., Bhattacharya, S. K., Shen, C. C. and Liang, M. C.: An insight
834 into the western Pacific wintertime moisture sources using dual water vapor isotopes, *J. Hydrol.*,
835 547, 111–123, doi:10.1016/j.jhydrol.2017.01.047, 2017.

836 Salamalikis, V., Argiriou, A. A. and Dotsika, E.: Isotopic modeling of the sub-cloud evaporation
837 effect in precipitation, *Sci. Total Environ.*, 544, 1059–1072, doi:10.1016/j.scitotenv.2015.11.072,

838 2016.

839 Salmon, O. E., Welp, L. R., Baldwin, M. E., Hajny, K. D., Stirm, B. H. and Shepson, P. B.:

840 Vertical profile observations of water vapor deuterium excess in the lower troposphere, *Atmos.*

841 *Chem. Phys.*, 19(17), 11525–11543, doi:10.5194/acp-19-11525-2019, 2019.

842 Steen-Larsen, H. C., Johnsen, S. J., Masson-Delmotte, V., Stenni, B., Risi, C., Sodemann, H.,

843 Balslev-Clausen, D., Blunier, T., Dahl-Jensen, D., Ellehøj, M. D., Falourd, S., Grindsted, A.,

844 Gkinis, V., Jouzel, J., Popp, T., Sheldon, S., Simonsen, S. B., Sjolte, J., Steffensen, J. P.,

845 Sperlich, P., Sveinbjörnsdóttir, A. E., Vinther, B. M. and White, J. W. C.: Continuous monitoring

846 of summer surface water vapor isotopic composition above the Greenland Ice Sheet, *Atmos.*

847 *Chem. Phys.*, 13(9), 4815–4828, doi:10.5194/acp-13-4815-2013, 2013.

848 Stewart, M. K.: Stable isotope fractionation due to evaporation and isotopic exchange of falling

849 waterdrops: Applications to atmospheric processes and evaporation of lakes, *J. Geophys. Res.*,

850 80(9), 1133–1146, doi:10.1029/JC080i009p01133, 1975.

851 Sun, C., Chen, W., Chen, Y. and Cai, Z.: Stable isotopes of atmospheric precipitation and its

852 environmental drivers in the Eastern Chinese Loess Plateau, China, *J. Hydrol.*, 581(November

853 2019), 124404, doi:10.1016/j.jhydrol.2019.124404, 2020.

854 Tan, L., An, Z., Huh, C.-A., Cai, Y., Shen, C.-C., Shiao, L.-J., Yan, L., Cheng, H. and Edwards,

855 R. L.: Cyclic precipitation variation on the western Loess Plateau of China during the past four

856 centuries, *Sci. Rep.*, 4(1), 6381, doi:10.1038/srep06381, 2014.

857 Thompson, L. G., Yao, T., Mosley-Thompson, E., Davis, M. E., Henderson, K. A. and Lin, P.-

858 N.: A High-Resolution Millennial Record of the South Asian Monsoon from Himalayan Ice Cores,

859 *Science* (80-.), 289(5486), 1916 LP – 1919, doi:10.1126/science.289.5486.1916, 2000.

860 Tian, C., Wang, L., Kaseke, K. F. and Bird, B. W.: Stable isotope compositions ($\delta^2\text{H}$, $\delta^{18}\text{O}$

861 and $\delta^{17}\text{O}$) of rainfall and snowfall in the central United States, *Sci. Rep.*, (October 2017), 1–

862 15, doi:10.1038/s41598-018-25102-7, 2018.

863 Wan, H., Liu, W. and Xing, M.: Isotopic composition of atmospheric precipitation and its tracing

864 significance in the Laohequ Basin, Loess plateau, China, *Sci. Total Environ.*, 640–641(May),

865 989–996, doi:10.1016/j.scitotenv.2018.05.338, 2018.

866 Wang, S., Zhang, M., Che, Y., Chen, F. and Fang, Q.: Contribution of recycled moisture to

867 precipitation in oases of arid central Asia: A stable isotope approach, *Water Resour. Res.*, 52(4),

868 3246–3257, doi:10.1002/2015WR018135, 2016a.

869 Wang, S., Zhang, M., Che, Y., Zhu, X. and Liu, X.: Influence of Below-Cloud Evaporation on

870 Deuterium Excess in Precipitation of Arid Central Asia and Its Meteorological Controls, *J.*

871 *Hydrometeorol.*, 17(7), 1973–1984, doi:10.1175/JHM-D-15-0203.1, 2016b.

872 Wang, S., Zhang, M., Hughes, C. E., Crawford, J., Wang, G., Chen, F., Du, M., Qiu, X. and

873 Zhou, S.: Meteoric water lines in arid Central Asia using event-based and monthly data, *J.*

874 *Hydrol.*, 562(May), 435–445, doi:10.1016/j.jhydrol.2018.05.034, 2018a.

875 Wang, Z., An, Z., Liu, Z., Qiang, X., Zhang, F. and Liu, W.: Hydroclimatic variability in loess

876 $\delta\text{D}_{\text{wax}}$ records from the central Chinese Loess Plateau over the past 250 ka, *J. Asian Earth*

877 *Sci.*, 155, 49–57, doi:https://doi.org/10.1016/j.jseaes.2017.11.008, 2018b.

878 Welp, L. R., Lee, X., Kim, K., Griffis, T. J., Billmark, K. A. and Baker, J. M.: $\delta^{18}\text{O}$ of water
879 vapour, evapotranspiration and the sites of leaf water evaporation in a soybean canopy, *Plant,*
880 *Cell Environ.*, 31(9), 1214–1228, doi:10.1111/j.1365-3040.2008.01826.x, 2008.

881 Wen, X. F., Zhang, S. C., Sun, X. M., Yu, G. R. and Lee, X.: Water vapor and precipitation
882 isotope ratios in Beijing, China, *J. Geophys. Res. Atmos.*, 115(1), 1–10,
883 doi:10.1029/2009JD012408, 2010.

884 Wu, H., Fu, C., Zhang, C., Zhang, J., Wei, Z. and Zhang, X.: Temporal Variations of Stable
885 Isotopes in Precipitation from Yungui Plateau: Insights from Moisture Source and Rainout Effect,
886 *J. Hydrometeorol.*, 23(1), 39–51, doi:10.1175/JHM-D-21-0098.1, 2022.

887 Wu, J., Li, P. and Qian, H.: Variation characteristics of meteorological elements and prediction
888 model of available precipitation in Xi'an city, *South-to-North water Transf. water Sci. Technol.*,
889 11(001), 50–54, 2013.

890 Xing, M., Liu, W., Li, X., Zhou, W., Wang, Q., Tian, J., Li, X., Tie, X., Li, G., Cao, J., Bao, H. and
891 An, Z.: Vapor isotopic evidence for the worsening of winter air quality by anthropogenic
892 combustion-derived water, *Proc. Natl. Acad. Sci.*, 117(52), 33005–33010,
893 doi:10.1073/pnas.1922840117, 2020.

894 Yao, T., Thompson, L. G., Mosley-Thompson, E., Zhihong, Y., Xingping, Z. and Lin, P.-N.:
895 Climatological significance of $\delta^{18}\text{O}$ in north Tibetan ice cores, *J. Geophys. Res. Atmos.*,
896 101(D23), 29531–29537, doi:10.1029/96JD02683, 1996.

897 Yao, T., Masson-Delmotte, V., Gao, J., Yu, W., Yang, X., Risi, C., Sturm, C., Werner, M., Zhao,
898 H., He, Y., Ren, W., Tian, L., Shi, C. and Hou, S.: A review of climatic controls on $\delta^{18}\text{O}$ in
899 precipitation over the Tibetan Plateau: Observations and simulations, *Rev. Geophys.*, 51(4),
900 525–548, doi:10.1002/rog.20023, 2013.

901 Zhao, L., Liu, X., Wang, N., Kong, Y., Song, Y., He, Z., Liu, Q. and Wang, L.: Contribution of
902 recycled moisture to local precipitation in the inland Heihe River Basin, *Agric. For. Meteorol.*,
903 271(July 2018), 316–335, doi:10.1016/j.agrformet.2019.03.014, 2019.

904 Zhu, G. F., Li, J. F., Shi, P. J., He, Y. Q., Cai, A., Tong, H. L., Liu, Y. F. and Yang, L.:
905 Relationship between sub-cloud secondary evaporation and stable isotope in precipitation in
906 different regions of China, *Environ. Earth Sci.*, 75(10), 876, 2016.

907